

Newtonian CAFE: a new ideal MHD code to study the solar atmosphere

J. J. González-Avilés¹ ^{*}, A. Cruz-Osorio² [†], F. D. Lora-Clavijo³ [‡] and F. S. Guzmán¹ [§]

¹*Instituto de Física y Matemáticas, Universidad Michoacana de San Nicolás de Hidalgo.*

Edificio C3, Cd. Universitaria, 58040 Morelia, Michoacán, México.

²*Instituto de Astronomía, Universidad Nacional Autónoma de México, AP 70-264, Distrito Federal 04510, México.*

³*Grupo de Investigación en Relatividad y Gravitación, Escuela de Física, Universidad Industrial de Santander, A. A. 678, Bucaramanga 680002, Colombia.*

17 October 2018

ABSTRACT

We present a new code designed to solve the equations of classical ideal magneto-hydrodynamics (MHD) in three dimensions, submitted to a constant gravitational field. The purpose of the code centers on the analysis of solar phenomena within the photosphere-corona region. We present 1D and 2D standard tests to demonstrate the quality of the numerical results obtained with our code. As solar tests we present the transverse oscillations of Alfvénic pulses in coronal loops using a 2.5 D model, and as 3D tests we present the propagation of impulsively generated MHD-gravity waves and vortices in the solar atmosphere. The code is based on high-resolution shock-capturing methods, uses the HLLE flux formula combined with Minmod, MC and WENO5 reconstructors. The divergence free magnetic field constraint is controlled using the Flux Constrained Transport method.

Key words: MHD - methods: numerical - Sun: atmosphere

1 INTRODUCTION

In solar physics one of the most important subjects is related to the dynamics of the plasma in the solar atmosphere. Specifically, phenomena which are related to the propagation of magnetohydrodynamic waves (e. g. Alfvén, slow, fast magnetoacoustic), and transients (e. g. vortices, jets, spicules). Recent observations based on data provided by current space missions, such as Transition Region and Coronal Explorer (TRACE), Solar Dynamics Observatory (SDO), Solar Optical Telescope (SOT), X-ray Telescope (XRT) and Swedish Solar Telescope (SST) (Banerjee et al. 2007; Tomczyk et al. 2007; De Pontieu et al. 2007; Okamoto et al. 2007; Jess et al. 2009) have enhanced the study of these phenomena in the solar atmosphere.

The type of effects in the solar atmosphere are considered when the plasma is fully ionized and therefore the ideal MHD equations represent a good model. However in this limit, these equations are highly non-linear and numerical simulations are essential, where accurate numerical algorithms play an important role. Over the recent years a number of codes have been used to understand various effects in

the solar atmosphere. For instance, in (Konkol & Murawski 2010; Danilko et al. 2012) the authors used a modification of ATHENA code (Stone et al. 2008) to study vertical oscillations of solar coronal loops and magnetoacoustic waves in a corollarygravitationally stratified solar atmosphere. In (Konkol et al. 2010; Murawski & Musielak 2010; Murawski et al. 2011; Murawski et al. 2013; Chmielewski et al. 2014a) the authors use a modification of the FLASH code (Fryxell et al. 2000; Lee & Deane 2009; Lee 2013) to simulate the propagation of MHD waves in two and three dimensions. Moreover in (Woloszkiewicz et al. 2014) the authors study the propagation of Alfvén waves in the solar atmosphere using the PLUTO code (Mignone et al. 2007).

Wave phenomena in the solar atmosphere have influenced the development of numerical codes dedicated specifically to study MHD wave propagation, e.g. the VAC code (Tóth 2000; Shelyag et al. 2008), which is capable to simulate the interaction of any arbitrary perturbation with a magnetohydrostatic equilibrium background. The SURYA code (Fuchs et al. 2011), allows to study the propagation of waves in a stratified non-isothermal magnetic solar atmosphere, in particular in the chromosphere-corona interface. Numerical simulations also permit to analyze some transient effects, for example in (Murawski & Zaqarashvili 2010; Murawski et al. 2011) using FLASH, the authors simulate the formation of spicules and macrospicules in the solar atmo-

^{*} E-mail: javiles@ifm.umich.mx (JJGA)

[†] E-mail: aosorio@astro.unam.mx (ACO)

[‡] E-mail: fadulora@uis.edu.co (FDLC)

[§] E-mail: guzman@ifm.umich.mx (FSG)

sphere. In addition in (Pariat et al. 2009; Pariat et al. 2010; Pariat et al. 2015) the authors propose a model for jet activity that is commonly observed in solar corona. Also the 3D ideal MHD equations are used to model the magnetic reconnection producing massive and high-speed jets (DeVore 1991).

Even though all the aforementioned codes are available, well documented and can be applied to various problems, we present our new application, with convergence tests and error analyses. Our code is at the moment useful to study solar phenomena in the photosphere-corona region, however with plan to generalize it to deal with magnetic reconnection and solar jets including radiative processes.

The paper is organized as follows. In Section 2 we describe the ideal MHD equations and mention the numerical methods implemented in our code. In Section 3 we show the standard tests in 1D and 2D dimensions. As a solar test in 2D we study the transverse oscillations of Alfvénic pulses in the solar coronal loops. We also present as a 3D test the propagation of MHD waves in a gravitationally non-isothermal solar atmosphere. Finally, in Section 4 we mention some final comments.

2 MHD EQUATIONS AND NUMERICAL METHODS

2.1 Ideal MHD Equations

We consider the set of the ideal MHD equations submitted to an external constant gravitational field. We choose to write down these equations in a conservative form, which is optimal for our numerical methods:

$$\frac{\partial \rho}{\partial t} + \nabla \cdot (\rho \mathbf{v}) = 0, \quad (1)$$

$$\frac{\partial(\rho \mathbf{v})}{\partial t} + \nabla \cdot (\rho \mathbf{v} \otimes \mathbf{v} - \mathbf{B} \otimes \mathbf{B} + \mathbf{I} p_t) = \rho \mathbf{g}, \quad (2)$$

$$\frac{\partial E}{\partial t} + \nabla \cdot ((E + p_t) \mathbf{v} - \mathbf{B}(\mathbf{v} \cdot \mathbf{B})) = \rho \mathbf{v} \cdot \mathbf{g}, \quad (3)$$

$$\frac{\partial \mathbf{B}}{\partial t} + \nabla \cdot (\mathbf{v} \otimes \mathbf{B} - \mathbf{B} \otimes \mathbf{v}) = \mathbf{0}, \quad (4)$$

$$\nabla \cdot \mathbf{B} = 0, \quad (5)$$

where ρ is the plasma mass density, $p_t = p + \frac{\mathbf{B}^2}{2}$ is the total (thermal + magnetic) pressure, \mathbf{v} represents the plasma velocity field, \mathbf{B} is the magnetic field, \mathbf{I} is the unit matrix and E is the total energy density, that is, the sum of the internal, kinetic, and magnetic energy density

$$E = \frac{p}{\gamma - 1} + \frac{\rho \mathbf{v}^2}{2} + \frac{\mathbf{B}^2}{2}. \quad (6)$$

The internal energy term is calculated considering an equation of state of an ideal gas

$$p = (\gamma - 1) \rho e, \quad (7)$$

where e is the internal energy density and γ is the adiabatic index. This equation also serves to close the system of equations (1)-(5). In solar surface problems one considers the gravitational source term given by $\mathbf{g} = [0, 0, -g]$ with

magnitude $g = 274 \text{ m/s}^2$, which is the value of the constant gravitational acceleration on the solar surface. These equations are written in units such that $\mu_0 = 1$. It is also convenient to write the equation of state in terms of the temperature, that is

$$p = \frac{k_B}{m} \rho T, \quad (8)$$

where k_B is Boltzmann's constant, m is the mean particle mass defined in terms of the mean atomic weight μ in the following way $\mu = m/m_p$, where m_p is the proton mass. The above mentioned system of equations (1)-(5) can be written as a first-order hyperbolic system of flux-conservative equations, which in cartesian coordinates reads

$$\begin{aligned} \frac{\partial \mathbf{Q}}{\partial t} + \frac{\partial \mathbf{F}}{\partial x} + \frac{\partial \mathbf{G}}{\partial y} + \frac{\partial \mathbf{H}}{\partial z} &= \mathbf{S}, \\ \nabla \cdot \mathbf{B} &= 0, \end{aligned} \quad (9)$$

with \mathbf{Q} a vector of conservative quantities

$$\mathbf{Q} = (\rho, \rho v_x, \rho v_y, \rho v_z, E, B_x, B_y, B_z)^T,$$

and \mathbf{F} , \mathbf{G} and \mathbf{H} are the fluxes along each spatial direction

$$\mathbf{F} = \begin{bmatrix} \rho v_x \\ \rho v_x^2 - B_x^2 + p_t \\ \rho v_x v_y - B_x B_y \\ \rho v_x v_z - B_x B_z \\ (E + p_t) v_x - B_x (\mathbf{B} \cdot \mathbf{v}) \\ 0 \\ v_x B_y - v_y B_x \\ v_x B_z - v_z B_x \end{bmatrix},$$

$$\mathbf{G} = \begin{bmatrix} \rho v_y \\ \rho v_y v_x - B_y B_x \\ \rho v_y^2 - B_y^2 + p_t \\ \rho v_y v_z - B_y B_z \\ (E + p_t) v_y - B_y (\mathbf{B} \cdot \mathbf{v}) \\ v_y B_x - v_x B_y \\ 0 \\ v_y B_z - v_z B_y \end{bmatrix},$$

$$\mathbf{H} = \begin{bmatrix} \rho v_z \\ \rho v_z v_x - B_z B_x \\ \rho v_z v_y - B_z B_y \\ \rho v_z^2 - B_z^2 + p_t \\ (E + p_t) v_z - B_z (\mathbf{B} \cdot \mathbf{v}) \\ v_z B_x - v_x B_z \\ v_z B_y - v_y B_z \\ 0 \end{bmatrix}.$$

Finally the source vector \mathbf{S} is given by

$$\mathbf{S} = \begin{bmatrix} 0 \\ 0 \\ 0 \\ -\rho g \\ -\rho v_z g \\ 0 \\ 0 \\ 0 \end{bmatrix}.$$

2.2 Characteristic Structure

The numerical methods used to solve the MHD equations require the characteristic information from the Jacobian matrices associated to the system of equations (9)

$$A_x(\mathbf{Q}) = \frac{\partial \mathbf{F}}{\partial \mathbf{Q}}, \quad A_y(\mathbf{Q}) = \frac{\partial \mathbf{G}}{\partial \mathbf{Q}}, \quad A_z(\mathbf{Q}) = \frac{\partial \mathbf{H}}{\partial \mathbf{Q}}.$$

As we can see, \mathbf{G} and \mathbf{H} can be obtained from an adequate index permutation of \mathbf{F} . Therefore, A_y and A_z have similar characteristic structure as A_x . The set of eigenvectors for the Jacobian matrices has been well established and extensively studied by several authors (Roe 1986; Brio & Wu 1988; Powell 1994; Ryu & Jones 1995; Balsara 2001). The corresponding eigenvalues for A_x , following the 8×8 eigen-system of Powell (Powell 1994; Powell et al. 1999) are given by

$$\lambda_{1,8} = v_x \pm c_f, \quad \lambda_{2,7} = v_x \pm c_a, \quad \lambda_{3,6} = v_x \pm c_s, \quad \lambda_{4,5} = v_x,$$

where c_a is the Alfvén speed

$$c_a = \sqrt{\frac{B_x^2}{\rho}},$$

c_f and c_s are the fast and slow magnetoacoustic speeds respectively

$$c_f = \left[\frac{1}{2} \left(a^2 + \frac{B^2}{\rho} + \sqrt{\left(a^2 + \frac{B^2}{\rho} \right)^2 - 4a^2 c_a^2} \right) \right]^{1/2},$$

$$c_s = \left[\frac{1}{2} \left(a^2 + \frac{B^2}{\rho} - \sqrt{\left(a^2 + \frac{B^2}{\rho} \right)^2 - 4a^2 c_a^2} \right) \right]^{1/2}$$

and $a = \sqrt{\frac{\gamma p}{\rho}}$ is the sound speed. Finally, similar expressions are found for A_y and A_z .

2.3 Numerical Methods

We solve numerically the magnetized Euler equations given by the system (1)-(5) on a single uniform cell centered grid, using the method of lines with a third order total variation diminishing Runge-Kutta time integrator (RK3) (Shu & Osher 1989). In order to use the method of lines, the right hand sides of MHD equations are discretized using a finite volume approximation with High Resolution Shock Capturing methods. For this, we first reconstruct the variables at cell interfaces using the Minmod and MC linear piecewise

second-order reconstructors, and the fifth-order weighted Essentially Non Oscillatory (WENO5) method (Titarev & Toro 2004; Harten A. et al. 1997; Radice & Rezzolla 2012), that uses a polynomial interpolation with a fifth order precision for smooth distributions and third order at strong shocks. Even though the accuracy of the RK3 dominates over a high order accuracy reconstructor during the time integration, we include WENO5 because it introduces a small amount of dissipation.

On the other hand, the numerical fluxes are built with the Harten-Lax-van-Leer-Einfeldt (HLLC) approximate Riemann solver formula, using the left and right states of the primitive and conservative reconstructed variables (Harten P. et al. 1983; Einfeldt 1988). The HLLC approximate solver uses a two-wave approximation to compute the fluxes across the discontinuity at the cell interfaces, including those of the magnetic and hydrodynamic waves. Such waves move with the highest and lowest velocities that correspond to eigenvalues of the Jacobian matrix. These numerical methods were implemented successfully in relativistic MHD, where we have studied different phenomena with fixed and dynamic background space-times, including the presence of black holes (Lora-Clavijo 2014; Lora-Clavijo et al. 2013; Lora-Clavijo et al. 2013b; Lora-Clavijo & Guzmán 2013; Cruz-Osorio et al. 2012; Lora-Clavijo & Cruz-Osorio 2015).

Additionally, in order to preserve the constraint (5) and avoid the violation of Maxwell’s equations (i.e. the development of unphysical results like the presence of magnetic charges) we use the flux constraint transport (flux-CT) algorithm (Evans & Hawley 1988; Balsara 2001). The flux-CT method is adapted to the conservative scheme computing the fluxes at cell vertex as an average of the fluxes at intercell boundaries and resulting in a cell-faced evolution equation of the components of the magnetic field. This scheme maintains the divergence of the magnetic field computed at cell corners to round-off accuracy along the numerical evolution. The details of the numerical implementation can be found in (Lora-Clavijo et al. 2015) and other divergence constraint control methods are summarized in (Tóth 2000).

3 NUMERICAL TESTS

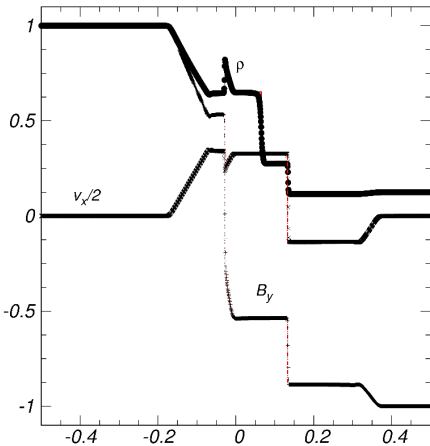
We include a set of 1D and 2D tests that involve the evolution with the gravitational field switched off. The solar tests include 2.5D and 3D tests involving the propagation of MHD waves in the solar atmosphere submitted to a constant gravitational field along the vertical direction.

3.1 1D tests

In order to illustrate how our implementation handles the evolution of a magnetized gas, in this subsection we present the standard shock tube tests in one direction. The 1D tests are Riemann problems under various initial conditions and we compare the numerical results with the exact solution calculated in (Takahashi & Yamada 2013; Takahashi & Yamada 2014).

We calculate the numerical solution of these tests using the HLLC formula and the various limiters mentioned, in the domain $[-0.5, 0.5]$ with $N = 1600$ identical cells, a constant Courant factor $CFL = 0.25$ for the first test, and

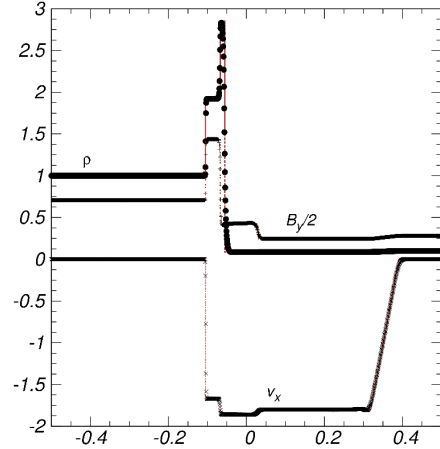
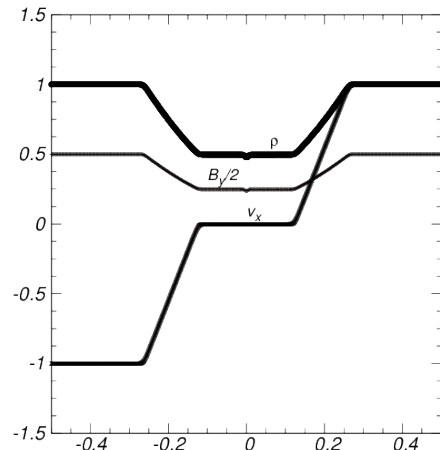
Test type	γ	ρ	p	v_x	v_y	v_z	B_x	B_y	B_z
Brio – Wu									
Left state	5/3	1.0	1.0	0.0	0.0	0.0	0.75	1.0	0.0
Right state		1.0	1.0	0.0	0.0	0.0	0.75	-1.0	0.0
Ryu&Jones 1b									
Left state	5/3	1.0	1.0	0.0	0.0	0.0	$3/\sqrt{4\pi}$	$5/\sqrt{4\pi}$	0.0
Right state		0.1	10.0	0.0	0.0	0.0	$3/\sqrt{4\pi}$	$2/\sqrt{4\pi}$	0.0
Ryu&Jones 2b									
Left state	5/3	1.0	1.0	0.0	0.0	0.0	$3/\sqrt{4\pi}$	$6/\sqrt{4\pi}$	0.0
Right state		0.1	10.0	0.0	2.0	1.0	$3/\sqrt{4\pi}$	$1/\sqrt{4\pi}$	0.0
Ryu&Jones 3b									
Left state	5/3	1.0	1.0	-1.0	0.0	0.0	0.0	1.0	0.0
Right state		1.0	1.0	1.0	0.0	0.0	0.0	1.0	0.0

Table 1. Parameters for the various MHD 1D Riemann problems.**Figure 1.** Test 1: Brio-Wu shock tube problem at $t = 0.1$. We show the numerical solution for ρ , v_x and B_y (points) and the exact solution (line). In this case we use the Minmod limiter.

0.05 for the others. The reason to choose this value is that in order to compare among reconstructors used here, we use a value that can be handled by all of them. The initial discontinuity in this case is located at $x = 0$. In order to estimate the error between the numerical solution and the exact solution, we calculate the numerical solution using four spatial resolutions $\Delta x_1 = 1/200$, $\Delta x_2 = 1/400$, $\Delta x_3 = 1/800$ and $\Delta x_4 = 1/1600$. For these tests we are using the 3D code with four cells along the transverse directions. The various parameters of 1D tests are summarized in Table 1 and we practiced this test for the three limiters mentioned.

3.1.1 Test 1: Brio-Wu Shock Tube Problem

The Brio-Wu MHD shock tube problem (Brio & Wu 1988) tests the capability of a code to handle waves of various types, shocks, rarefactions, contact discontinuities and the compound structures of MHD. A snapshot of the wave structure at $t = 0.1$ of the solution is shown in Fig. 1. The left-moving fast rarefaction wave from $x \approx -0.2$ to $x \approx -0.1$ and the slow compound wave at $x \approx -0.03$ are well captured. The contact discontinuity is captured at $x \approx 0.05$. Finally the slow shock is captured at $x \approx 0.15$ and fast rarefaction from $x \approx 0.32$ to $x \approx 0.37$.

**Figure 2.** Test 2: Ryu & Jones 1b shock tube problem at $t = 0.03$. We show the numerical solution for ρ , v_x and B_y (points) compared with the exact solution (line). Again we use the Minmod limiter.**Figure 3.** Test 3: Ryu & Jones 3b shock tube problem at $t = 0.1$. We show the numerical solution for ρ , v_x and magnetic field B_y (points) compared with the exact solution (line).

3.1.2 Test 2: Ryu & Jones 1b

This test was introduced by (Ryu & Jones 1995). It is important to check on the ability of the numerical scheme to handle a fast shock, a rarefaction shock, a slow shock, a slow rarefaction, and a contact discontinuity. A snapshot of the evolution is displayed in Fig. 2. Our results show that fast shock at $x \approx -0.11$ and the slow shock at $x \approx -0.075$ are well captured. In addition the contact discontinuity appears at $x \approx -0.061$ and the slow rarefaction is located at $x \approx -0.040$. Finally the fast rarefaction is captured at $x \approx 0.34$.

3.1.3 Test 3: Ryu & Jones 3b

This is a test containing magnetosonic rarefactions waves. The numerical solution shows only two strong and identical magnetosonic rarefactions. Our code was able to capture this structure and the results are shown in Fig. 3.

3.1.4 Error estimates for the 1D MHD tests

In order to compare the numerical solutions using different limiters implemented in our code, we have calculated the error for each 1D Riemann test described above, and the results are summarized in Table 2. In all the tests, with the three reconstructors used, our runs lie within the consistency regime, that is, the error decreases when resolution is increased. In order to go further we check for the order of convergence. For this we calculate the L_1 norm of the error as compared with the exact solution. Since we always consider resolution factors of two, the order of convergence is given by $\log(\text{error}_i/\text{error}_{i-1})/\log(2)$, where i is the error calculated with the resolution Δx_i . Thus we carried out the tests with four spatial resolutions. For all the tests we obtained near first order convergence as expected, considering all the initial data start with discontinuities and in Table 2 we show how the different reconstructors perform in the different tests.

3.2 2D tests

3.2.1 Orszag-Tang Vortex

The Orszag Tang vortex system was first studied by (Orszag & Tang 1998). This is a well known problem for testing the transition to a supersonic 2D MHD turbulence, and to measure the robustness of the code at handling the formation of MHD shocks. The important dynamics developed during the evolution is a test for the controller of the magnetic field divergence free constraint $\nabla \cdot B = 0$.

The initial data are $\mathbf{v} = v_0(-\sin(2\pi y), \sin(2\pi x), 0)$, $\mathbf{B} = B_0(-\sin(2\pi y), \sin(4\pi x), 0)$, $\rho_0 = 25/(36\pi)$ and $p_0 = 5/(12\pi)$, where $v_0 = 1$ and $B_0 = 1/\sqrt{4\pi}$ with $\gamma = 5/3$, are defined in such a way that the system develops a vortex. The initial data for ρ and p are calculated using averaged β and the Mach number M (Dai & Woodward 1998), which are defined as

$$\beta = \frac{p_0}{\langle \mathbf{B}^2 \rangle / 8\pi} = 8\pi p_0,$$

$$M = \frac{\langle \mathbf{u}^2 \rangle}{c_s^2} = \frac{\rho_0}{\gamma p_0}.$$

In this case $\beta = 10/3$ and $M = 1$. We carry out the evolution on the domain $[0, 1] \times [0, 1]$ that we cover with 512×512 cells, and impose periodic boundary conditions.

The evolution of the density shows the development of turbulence and the interaction of the shock within the domain as shown in the snapshots taken at times $t = 0.5$ and $t = 1.0$ in Fig. 4, which can be compared with the results from ATHENA (Stone et al. 2008). Our code maintains the constraint on values $|\nabla \cdot B| \approx 10^{-13}$, which is within the round-off error of the machine accuracy. In order to show how the fluid makes the transition to a supersonic turbulence, we calculate the Mach number defined as $M = |v|^2/c_s^2$, where $|v|^2 = v_x^2 + v_y^2$, where $c_s^2 = \frac{\gamma p}{\rho}$ is the speed of sound. Snapshots taken at times $t = 0.5$ and $t = 1$ of M are shown in Fig. 5, where we can see that Mach number increases in regions where the density decreases. More quantitative results are shown in Fig. 6, where the pressure with various resolutions is measured on the line $y = 0.3125$ at time

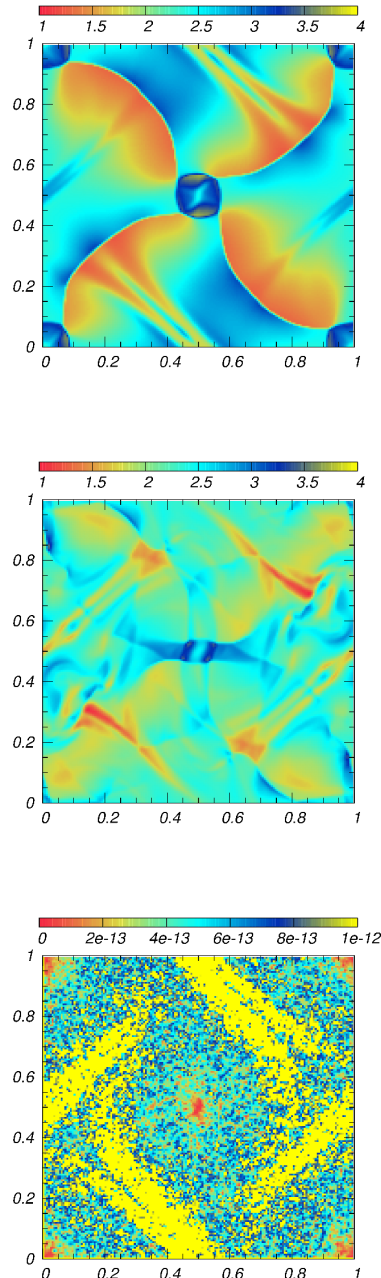


Figure 4. Density for the Orszag-Tang vortex at times $t = 0.5$ (top) and $t = 1.0$ (middle). We show $|\nabla \cdot B|$ at $t = 1.0$ in the xy plane (bottom).

$t = 0.5$. The results are shown for the Minmod reconstructor and are in agreement with those in Fig. 11 of (Londrillo & Del Zanna 2000). Moreover, the results can be compared with those using FLASH (Fryxell et al. 2000; Lee & Deane 2009; Lee 2013), ATHENA (Stone et al. 2008) and PLUTO (Mignone et al. 2007).

<i>Resolution</i>	MM	MC	WENO5	MM	MC	WENO5
Error			Order of convergence			
Brio – Wu						
Δx_1	0.11e-1	0.11e-1	0.82e-2
Δx_2	0.66e-2	0.66e-2	0.45e-2	0.74	0.74	0.86
Δx_3	0.41e-2	0.41e-2	0.28e-2	0.69	0.69	0.68
Δx_4	0.25e-2	0.25e-2	0.19e-2	0.71	0.71	0.55
Ryu&Jones 1b						
Δx_1	0.32e-1	0.27e-1	0.24e-1
Δx_2	0.22e-1	0.15e-1	0.13e-1	0.71	0.84	0.88
Δx_3	0.14e-1	0.80e-2	0.74e-2	0.65	0.90	0.81
Δx_4	0.86e-2	0.50e-2	0.45e-2	0.70	0.67	0.71
Ryu&Jones 3b						
Δx_1	0.71e-2	0.46e-2	0.43e-2
Δx_2	0.37e-2	0.23e-2	0.22e-2	0.94	1.0	0.96
Δx_3	0.19e-2	0.12e-2	0.12e-2	0.96	0.93	0.87
Δx_4	0.10e-2	0.67e-3	0.79e-3	0.92	0.84	0.60

Table 2. L_1 norm of the error in density calculated with four resolutions and three numerical reconstructors. We also show the order of convergence between the different pairs of resolutions.

3.2.2 The circularly polarized Alfvén Wave Test

This test problem was presented in (Tóth 2000). The circularly polarized wave is an exact nonlinear solution to the MHD equations, which allows one to test a code in the nonlinear regime. This test is useful to measure the ability of the numerical scheme to describe the propagation of Alfvén waves. The initial data of this problem are $\rho = 1$, $p = 0.1$, $v_\perp = 0.1 \sin(2\pi x_\parallel)$, $v_\parallel = 0$, $B_\perp = 0.1 \sin(2\pi x_\parallel)$, $B_\parallel = 1$, $v_z = 0.1 \cos(2\pi x_\parallel)$, $B_z = 0.1 \cos(2\pi x_\parallel)$, where $x_\parallel = (x \cos \alpha + y \sin \alpha)$ and $\alpha = 30^\circ$ is the angle at which the wave propagates with respect to the grid. Here v_\perp and B_\perp are the components of velocity and magnetic field perpendicular to the wavevector. The Alfvén speed is $|v_A| = B_\parallel/\rho = 1$, which implies that at time $t = 1$ the flow is expected to return to its initial state.

The domain $[0, 1/\cos \alpha] \times [0, 1/\sin \alpha]$ is covered with 256×256 cells. In order to see that our code is capable to describe the propagation of circularly polarized Alfvén waves along the diagonal grid, in Fig. 7 (top) we show a snapshot of B_\perp as function of v_\parallel taken at time $t = 5$ for 6 different resolutions in the case of a travelling wave ($v_\parallel = 0$) (top), in this case the diffusion of the wave is less for a higher resolution as expected. We also show a snapshot of B_z taken at time $t = 5$, where one can notice that the wavefronts remain planar despite the propagation occurs along a non-preferred grid direction. Again the code maintains $|\nabla \cdot B| \approx 10^{-13}$ as shown in Fig. 7. In this test we use Minmod and the

results can be compared with those obtained with ATHENA (Stone et al. 2008).

3.2.3 Current Sheet Test problem

This two dimensional problem was presented in (Hawley & Stone 1995) and is important because it shows the ability of the code to deal with magnetic reconnection driven solely by numerical resistivity. Additionally, the fact that magnetic reconnection produces high pressure gradients this test also serves to monitor the behavior of the code when dealing with these sharp gradients.

The computational domain $[-0.5, 0.5] \times [-0.5, 0.5]$ is covered with 600×600 cells. We use the Minmod reconstructor and impose periodic boundary conditions in all sides. We initialize the two current sheets as follows:

$$B_y = \begin{cases} B_0 & \text{for } |x| > 0.25 \\ -B_0 & \text{otherwise,} \end{cases}$$

where $B_0 = 1$. The other magnetic field components B_x , B_z are set to zero. The velocity is $\mathbf{v} = (u_0 \sin(2\pi y), 0, 0)$ with $u_0 = 0.1$. The density $\rho = 1$ and the gas pressure $p = \beta/2$, in this case we choose $\beta = 0.1$. The problem is initialized with a magnetic field along the y direction, that switches signs twice in the domain. This system is then perturbed with a sinusoidal velocity function, which initially creates nonlinear polarized Alfvén waves. These waves quickly turn into

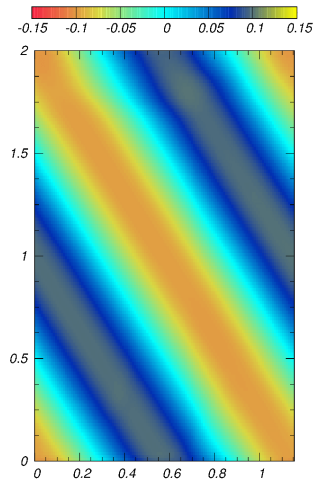
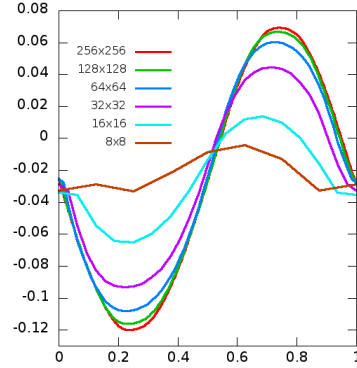
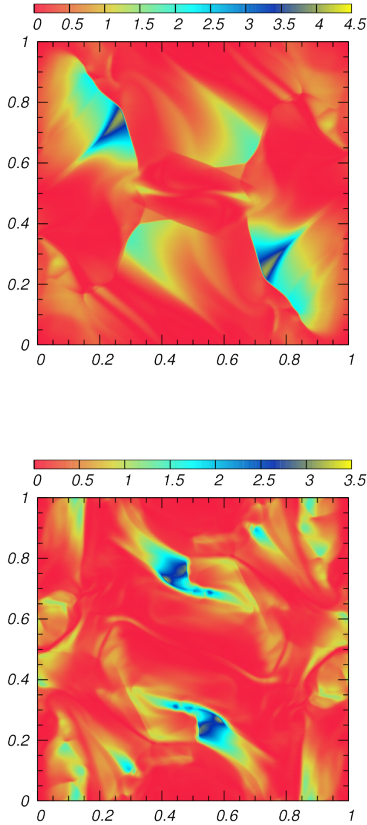


Figure 5. Mach number M for the Orszag-Tang vortex at times $t = 0.5$ (top) and $t = 1.0$ (bottom) in the xy plane. The supersonic regions are located in the dark colored zones.

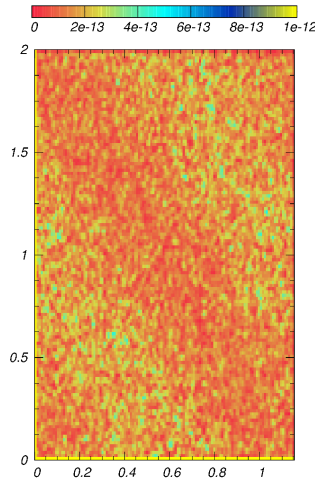
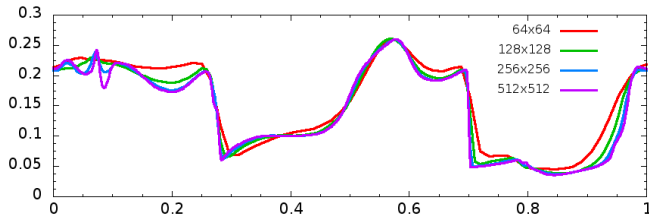


Figure 6. Horizontal slices of p along $y = 0.3125$ for the Orszag-Tang vortex using four spatial resolutions using Minmod. This plot shows the consistency of the solution.

Figure 7. Circularly polarized Alfvén wave test. We show the perpendicular component of magnetic field B_{\perp} as a function of x_{\parallel} at time $t = 5$, using six resolutions (top), B_z at time $t = 5$ (middle) and $|\nabla \cdot B|$ at $t = 5$ (bottom) in the xy plane.

magnetosonic waves. Eventually, numerical reconnection occurs between the field lines as shown in Fig. 8 (bottom-left), which causes magnetic energy to be turned into thermal energy. This process can be seen in the plots of Fig. 8, which show regions of high gas pressure and low magnetic pressure, these regions appear in the form of bubbles which eventually merge with each other. Moreover, even though reconnection takes place, the constraint is kept under control $|\nabla \cdot B| \approx 10^{-12}$. The results can be compared with those using FLASH (Fryxell et al. 2000; Lee & Deane 2009; Lee 2013) and ATHENA (Stone et al. 2008).

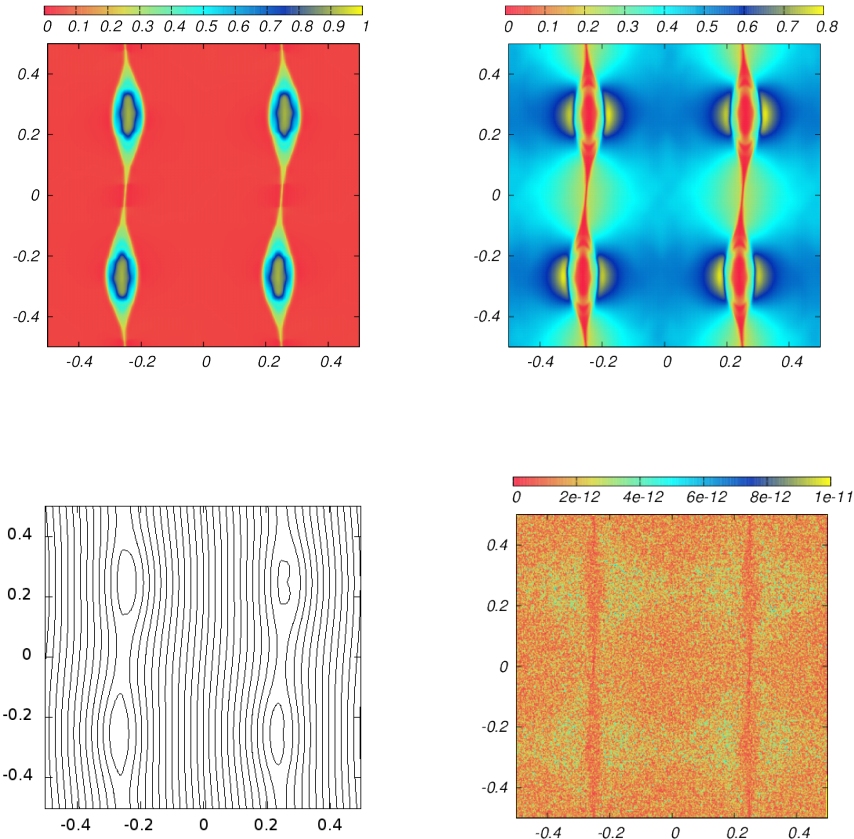


Figure 8. Current sheet test. We show gas pressure p , magnetic pressure $B^2/2$, magnetic field lines and $|\nabla \cdot B|$ at time $t = 1.5$ in the xy plane.

3.3 Solar Tests

In order to show that our code can handle solar physics problems in the gravitationally stratified solar atmosphere, we study the transverse oscillations of Alfvénic pulses in solar coronal loops using a 2.5 D model, and in the case of a 3D configuration, we study the propagation of impulsively generated magnetohydrodynamic-gravity waves and vortices in the gravitationally stratified non-isothermal solar atmosphere.

3.3.1 Transverse oscillations in solar coronal loops

Following the idea developed in (Del Zanna et al. 2005), we study impulsively generated Alfvén waves propagating in a magnetic arcade, taking into account a stratified solar atmosphere with height from the photosphere-corona region in order to study transverse oscillations in coronal loops. These oscillations are considered due to flare events generally interpreted as standing kink oscillations.

In this problem, the model of the coronal arcade is obtained from a solution of the static 2D MHD equations (Priest 1982), and is given by:

$$\begin{aligned} B_x &= B_0 \cos(kx) \exp(-kz), \\ B_z &= -B_0 \sin(kx) \exp(-kz), \end{aligned} \quad (10)$$

where $B_0 = 40$ G is the photospheric field magnitude at the footpoints $x = \pm L/2$ and $k = \pi/L$. We choose in our set up to use $L = 50$ Mm. This is a force and current free magnetic field, which implies that the pressure gradient must simply balance gravity in the vertical direction, that is, according to (2)

$$-\nabla p_e + \rho_e \mathbf{g} = \mathbf{0}. \quad (11)$$

Using the equation of state for a fully ionized hydrogen plasma $p = 2k_B \rho T / m_p$, we obtain the thermal pressure:

$$p(z) = p(z_0) \exp\left(-\frac{m_p g}{2k_B} \int_{z_0}^z \frac{dz'}{T(z')}\right), \quad (12)$$

where $p(z_0)$ is the pressure at photospheric level. Then the mass density is calculated using the equation of state (8) and gives $\rho(z) = \frac{m_p p(z)}{2k_B T(z)}$. In this problem the temperature model for the solar atmosphere is given by a smoothed step function

$$T(z) = \frac{1}{2}T_{cor} \left(1 + dtc + (1 - dtc) \tanh \left(\frac{z - z_t}{z_w} \right) \right), \quad (13)$$

where $dtc = T_{phot}/T_{cor}$ and $T_{phot} = 6000$ K is the temperature at the photosphere, $T_{cor} = 1.2 \times 10^6$ K is the higher coronal temperature. These two regions are separated at $z_t = 2$ Mm by a transition region of width $z_w = 0.2$ Mm. With this profile we integrate (12) to obtain the pressure and therefore the density.

Following (Del Zanna et al. 2005), in order to simulate impulsively generated Alfvén waves, we add a purely transversal velocity pulse v_y at initial time $t = 0$, located at (x_0, z_0) :

$$v_y = \frac{Av_0}{1 + (r/r_0)^4}, \quad (14)$$

where $r = \sqrt{(x - x_0)^2 + (z - z_0)^2}$ with $x_0 = 0$ Mm and $z_0 = 50$ Mm, $A = 0.1$ is the normalized amplitude, $v_0 = 1$ Mm/s is the typical Alfvén speed in the corona and $r_0 = 1$ Mm. Therefore the initial conditions for this problem are given by: $p = p(z)$, $\rho = \rho(z)$, the velocity field $\mathbf{v} = (0, v_y, 0)$, and $\mathbf{B} = (B_x, 0, B_z)$.

We solve the equations (1)-(5) using the Minmod slope limiter, a Courant factor $CFL=0.2$ and $\gamma = 5/3$. We set the simulation domain to $[-25, 25] \times [0, 1] \times [0, 50]$ Mm³, covered with $400 \times 4 \times 400$ cells, and we impose open boundary conditions in all faces.

We consider the case of a symmetric pulse given by the equation (14). In Fig. 9 we show snapshots of the transverse velocity v_y at times $t = 10$ s, $t = 40$ s, $t = 100$ s and $t = 200$ s. At time $t = 10$ s we can see the propagation of two Alfvénic pulses with the same amplitude move downward following the fieldlines of coronal loop. At time $t = 40$ s the pulses have passed transition region where their amplitude decrease. The pulses move in regions with low density at time $t = 100$ s, so the pulses assume a elongated shape. At time $t = 200$ s the pulses hit the transition region twice and came back to the center of domain. In this time it is clear the spreading of the pulse, that goes together with a high amplitude decrease produce by reflection at the transition region. Even though the complex dynamics of the Alfvénic pulses, the $\nabla \cdot \mathbf{B}$ is maintained in the order of 10^{-12} Tesla/km as is shown in Fig. 9 (bottom).

3.3.2 Propagation of magnetohydrodynamic-gravity waves in the 3D solar atmosphere

Following (Murawski et al. 2013), we simulate the evolution magnetohydrodynamic-gravity waves and the vortex formation in the magnetized three-dimensional (3D) solar atmosphere. Initially we assume the solar atmosphere to be in static equilibrium (Murawski & Musielak 2010; Murawski & Zaqarashvili 2010; Murawski et al. 2011; Woloszkiewicz et al. 2014; Chmielewski et al. 2014a; Chmielewski et al. 2014b; González-Avilés & Guzmán 2015), and the initial equilibrium magnetic field \mathbf{B}_e constant along the vertical direction

$$\mathbf{B}_e = B_0 \hat{\mathbf{z}}, \quad (15)$$

where $B_0 = 23$ G, which is a value close to a typical magnetic field magnitude in the quiet Sun (Vögler & Schüssler 2007).

As a result of applying the static equilibrium and the magnetic current-free conditions to equation (2), the pressure gradient is balanced by gravity through equation (11). In addition, considering the fact that hydrostatic equilibrium will only hold along the z direction, the equilibrium gas pressure takes the form:

$$p_e(z) = p_{ref} \exp \left(- \int_{z_{ref}}^z \frac{dz'}{\Lambda(z')} \right), \quad (16)$$

and the mass density

$$\rho_e(z) = \frac{p_e(z)}{g\Lambda(z)}, \quad (17)$$

where

$$\Lambda(z) = \frac{k_B T_e(z)}{mg}, \quad (18)$$

is the pressure scale-height, and p_{ref} represents the gas pressure at a given reference level, that we choose to be located at $z_{ref} = 10$ Mm, because in the temperature model above, this is the location at which the corona region starts. In this case we use $\mu = 1.24$ in (8) only to reproduce the results in (Murawski et al. 2013).

The temperature field $T_e(z)$ is assumed to obey the C7 model (Avrett & Loeser 2008), which is a semiempirical model of the chromosphere. This C7 temperature profile was interpolated into the 3D numerical grid, then we numerically integrated equation (16) in order to obtain $p_e(z)$ and finally with this profile we use equation (17) to obtain $\rho_e(z)$. We show the temperature and density profile in Fig. 10 where the important density gradients can be observed. In addition we show the plasma β to see how the magnetic pressure dominates over gas pressure in the solar atmosphere.

In order to simulate the propagation of magnetohydrodynamic-gravity waves, we perturb the static solar atmosphere with a Gaussian pulse, either in the horizontal component of velocity, v_x , or in the vertical component v_z . Following (Murawski et al. 2013), the initial conditions are given by

$$v_x(x, y, z, t = 0) = A_v e^{-\frac{x^2 + y^2 + (z - z_0)^2}{w^2}}, \quad (19)$$

$$v_z(x, y, z, t = 0) = A_v e^{-\frac{x^2 + y^2 + (z - z_0)^2}{w^2}}, \quad (20)$$

where A_v is the amplitude of the pulse, z_0 is the initial position over the vertical direction and w denotes the width of the pulse. In this case we use the values $A_v = 3$ kms⁻¹, $w = 100$ km and $z_0 = 500$ km. Therefore the initial conditions for this problem are given by: $p = p_e(z)$, $\rho = \rho_e(z)$, the velocity field $\mathbf{v} = (v_x, 0, v_z)$ depends on the direction of perturbation, and $\mathbf{B} = (0, 0, B_0)$.

We solve the equations (1)-(5) using the HLLC Riemann solver, the Minmod slope limiter, a Courant factor $CFL=0.2$ and $\gamma = 1.4$. We set the simulation domain to $[-0.75, 0.75] \times [0, 3] \times [-0.75, 0.75]$ Mm³, covered with $64 \times 128 \times 64$ cells for the case of horizontal perturbation and $100 \times 200 \times 100$ cells for vertical perturbation. At the top and

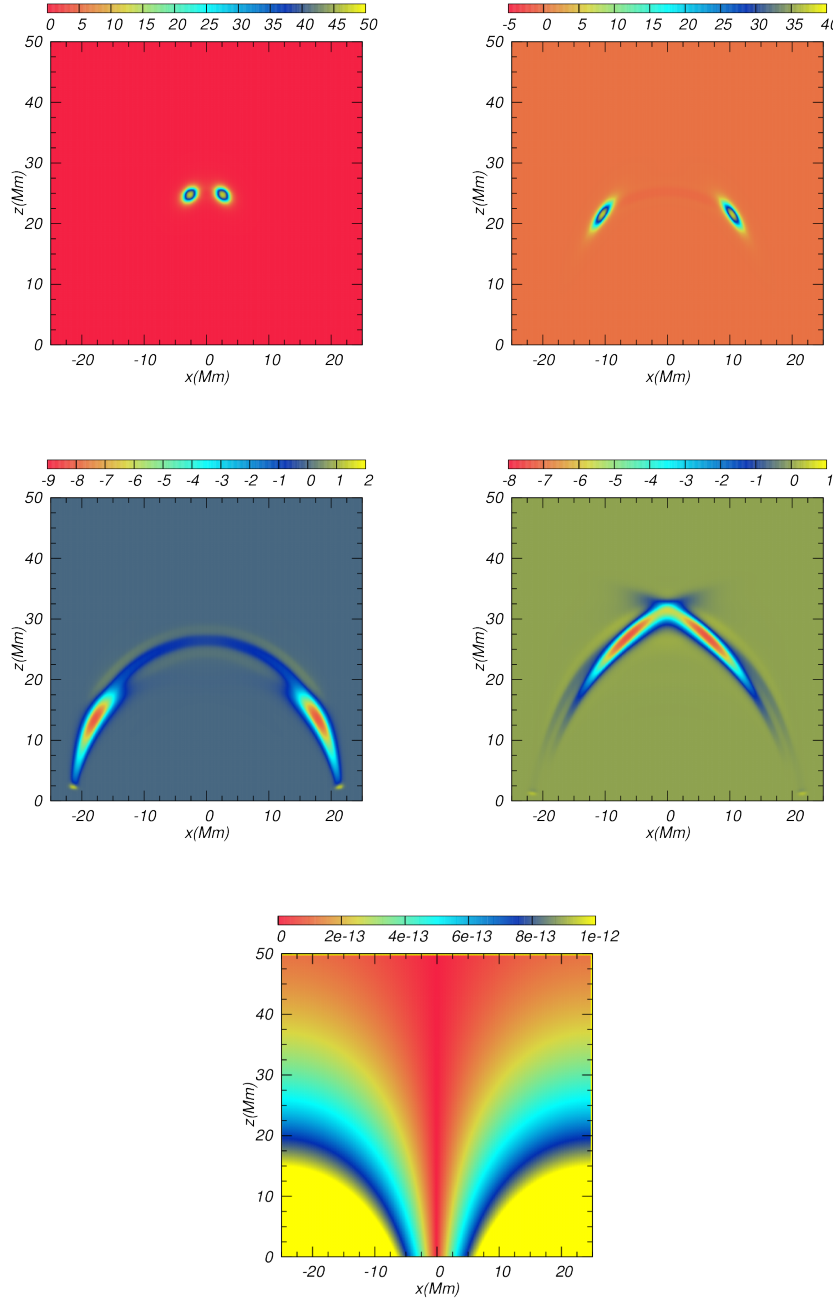


Figure 9. Transverse velocity v_y (km/s) at times $t = 10$ s, $t = 40$ s, $t = 100$ s, $t = 200$ s and $\nabla \cdot B$ (Tesla/km) at $t = 200$ s.

bottom faces of the numerical domain we impose fixed in time boundary conditions, whereas at the remaining four sides we apply open boundary conditions. In our simulations we choose the scale factors in cgs units as specified in Table 3. These units are obtained choosing a length-scale l_0 , plasma density scale ρ_0 and magnetic field scale B_0 , this fixes the unit of time in terms of Alfvén speed as follows:

$$B_0 = v_0 \sqrt{\mu_0 \rho_0}, \quad (21)$$

where $\mu_0 = 4\pi \times 10^{-7} \text{ N/A}^2$ is the magnetic permeability

and $\rho_0 = 10^{-12} \text{ kg/m}^3$ is the plasma scale at the level of the solar corona.

3.3.3 Vertical perturbation

Vertical perturbations in the sun could be generated by p -modes (Jain R. et al. 2011), which are pressure or acoustic modes with frequencies greater than 1 mHz. This kind of perturbation is given by the component v_z in equation (20). The initial pulse triggers longitudinal magnetoacoustic-gravity waves. At the initial point where the wave is

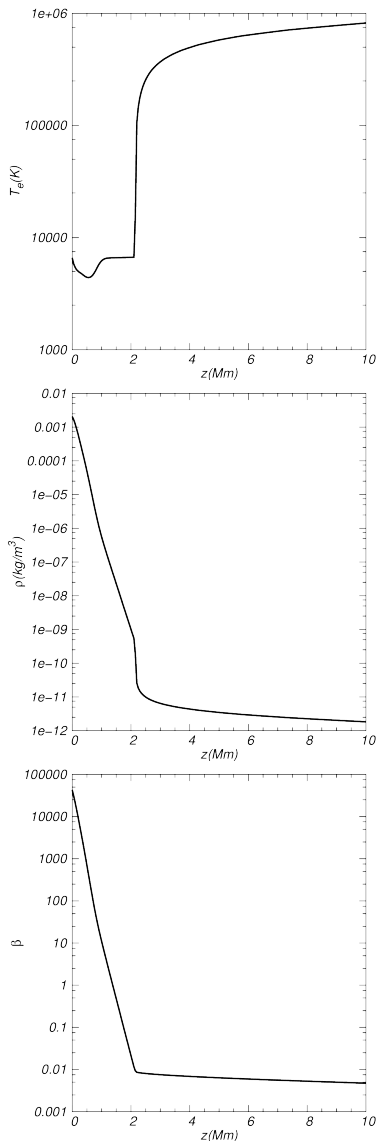


Figure 10. Temperature, density and β profile for the C7 model.

Table 3. Units used in this paper

Quantity	cgs units
l_0	10^8 cm
v_0	10^8 cm·s $^{-1}$
t_0	1 s
ρ_0	10^{-15} gr·cm $^{-3}$
B_0	11.21 G

launched, the gas pressure is greater than the magnetic pressure, which implies that $\beta > 1$. This excites fast and slow magnetoacoustic-gravity waves which are coupled. The initial pulse splits into two propagating waves at time $t = 37.5$ s shown in Fig. 11 (top). At time $t = 100$ s, the two magnetoacoustic waves move upwards until $z \approx 1.4$ Mm, in the same way as in Fig. 3 of (Murawski et al. 2013). The waves continue moving until they reach the transition re-

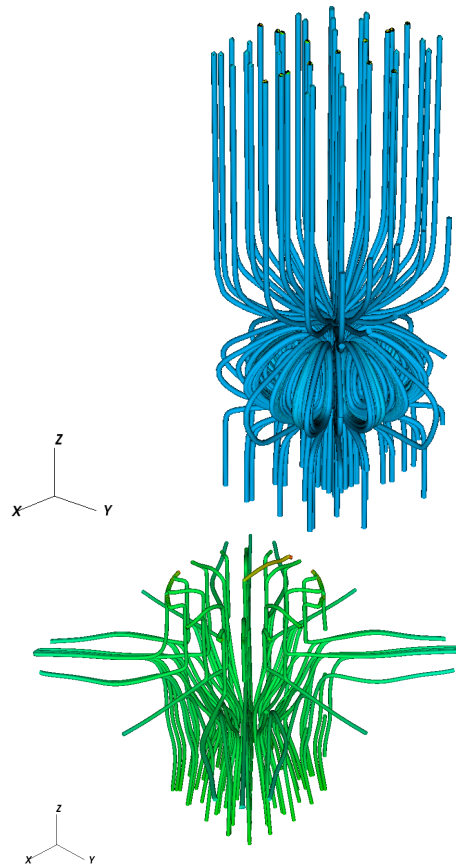


Figure 13. Temporal snapshots of streamlines at $t = 37.5$ s (top) and $t = 150$ s (bottom) for the case of vertical perturbation. Color represents the vorticity magnitude.

gion. This vertical perturbation produces the propagation of magnetoacoustic-gravity waves in a symmetric way, as shown in Fig. 11 at the xz and yz planes. In these two planes the propagation is seen in the same way. We also show the propagation as seen from above, on the xy plane in Fig. 12. Even though the structure of the magnetoacoustic-gravity waves in the solar atmosphere looks complex, the value of $|\nabla \cdot B|$ at time $t = 150$ s in the xy plane remains low as is shown in Fig. 12.

We show snapshots of the fluid streamlines at times $t = 37.5$ s and $t = 150$ s in Fig. 13. These streamlines reveal vortices specially at time $t = 37.5$ s, which are produced by the vertical perturbation v_z and are located at 1 Mm over the photosphere.

3.3.4 Horizontal perturbation

Horizontal perturbations in the solar atmosphere can be generated due to granular cells as a result of convection toward the photosphere. In this case we simulate these waves by exciting the v_x component in equation (19). This initial pulse excites all MHD waves which are affected by the gravitational constant field. Since early times we can see the magnetoacoustic-gravity waves propagating upwards in the xz plane as light yellow wave-fronts in Fig. 14 (top). At time $t = 150$ s we can see the magnetoacoustic-gravity waves light

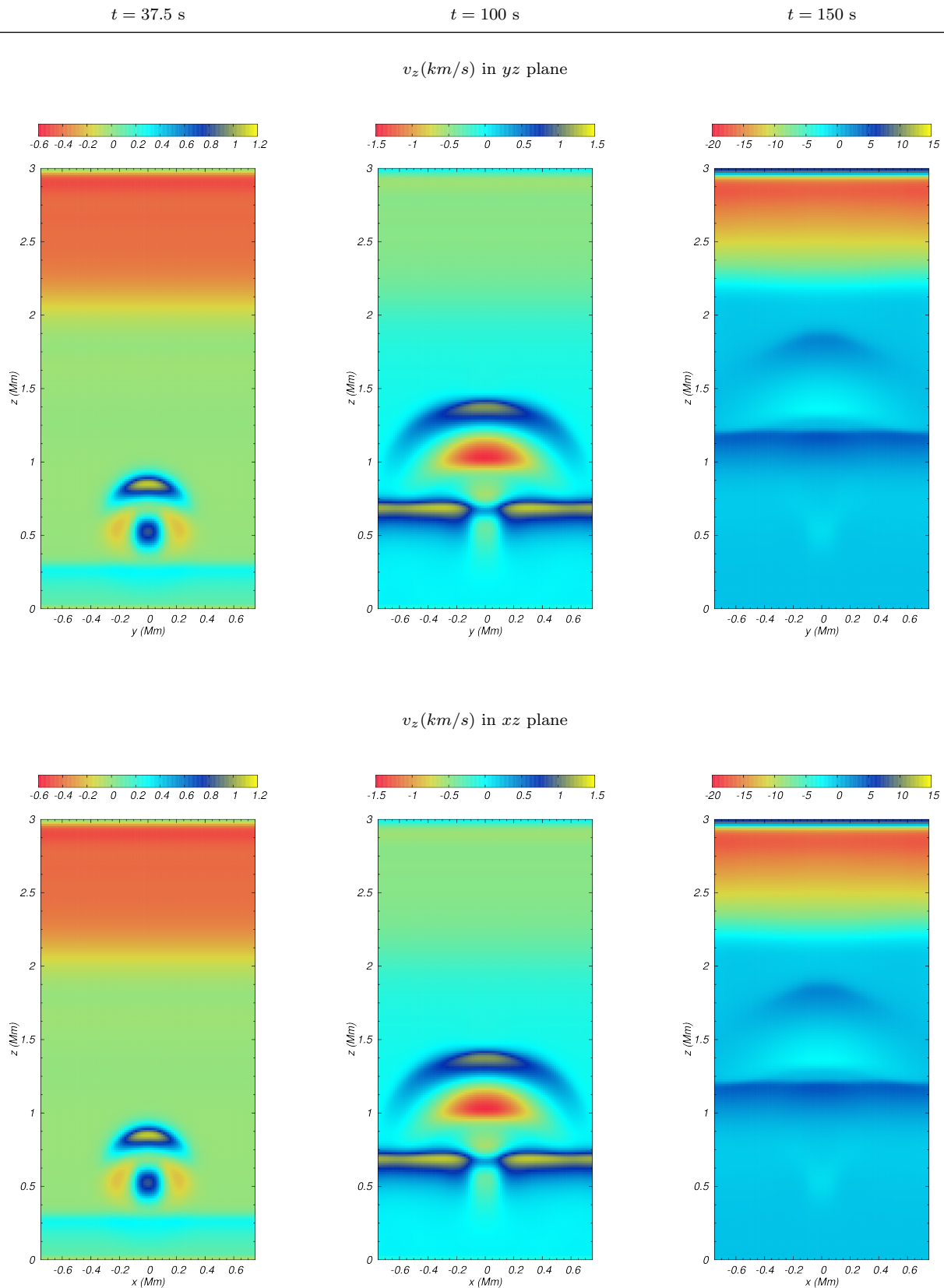


Figure 11. Snapshots of the vertical component of velocity v_z (km/s) at times $t = 37.5, 100, 150$ s in the yz and xz planes.

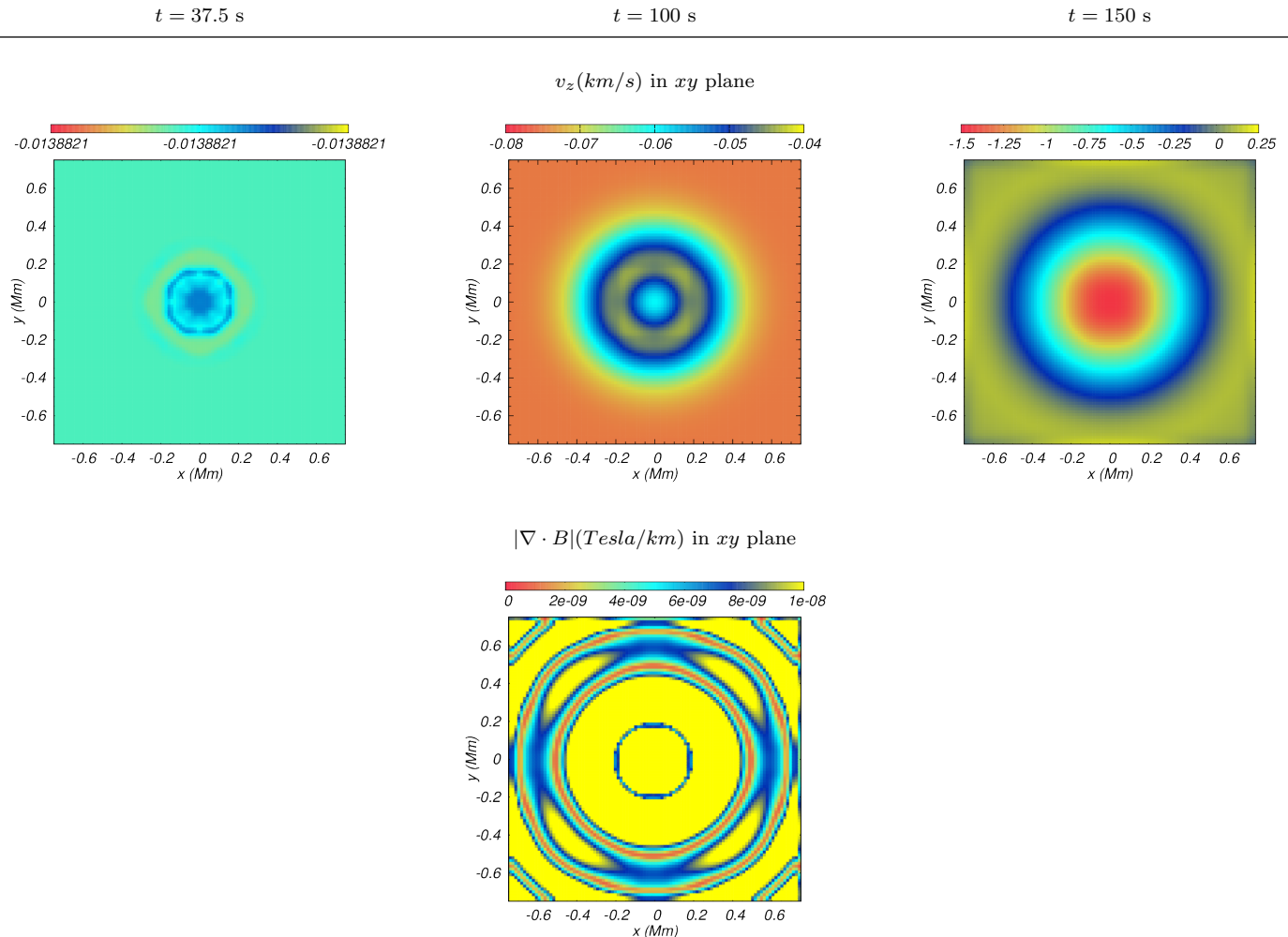


Figure 12. Snapshots of the vertical component of velocity v_z (km/s) at times $t = 37.5, 100, 150$ s and $|\nabla \cdot B|$ at $t = 150$ s in the xy plane.

yellow patches reaching the level $z = 1.75$ Mm as shown in the top of Fig. 6 of (Murawski et al. 2013). At time $t = 250$ s, the waves reach the transition region, which causes the appearance of a light blue patch in Fig. 14, but later on, they are reflected back. In order to see the propagation of the waves from different planes, we show v_x projected on the xz and yz planes in Fig. 14 (bottom). Unlike the previous test, in this case the velocity is not symmetrical. Moreover, the propagation of the waves seen from above show how the wave-fronts change their amplitudes until the reflection happens, this is shown in the top panel of Fig. 15. As in the previous case we show a snapshot of $|\nabla \cdot B|$ at time $t = 150$ s in Fig. 15 (bottom).

In this case we also show snapshots of the fluid streamlines at times $t = 50$ s and $t = 150$ s in Fig. 16. In the same way as in the case of the vertical perturbation, the horizontal perturbation generates vortices, but in this case the vorticity is more complex. It has been proposed that vortices are triggered by convective or granular motions (Murawski et al. 2013).

4 FINAL COMMENTS

We have presented a new code that solves the ideal MHD equations intended to model phenomena in the solar atmosphere.

We have included standard 1D Riemann problem tests and shown that the order of convergence lies within the expected range corresponding to the methods we use. We conclude from our analysis, that MC and WENO5 perform better than the Minmod limiter.

We have also presented standards 2D tests including the Orszag-Tang vortex and a current sheet test problem showing magnetic reconnection. In these tests we have kept the magnetic field divergence free constraint under control, in all the tests near round-off error. We notice that, according to previous experience, due to the dissipation, Minmod performs well and the MC and WENO5 limiters allow more refined structures in general.

The solar tests have been oriented to study wave propagation in a gravitationally stratified solar atmosphere. We track the transverse oscillations of Alfvénic pulses in solar

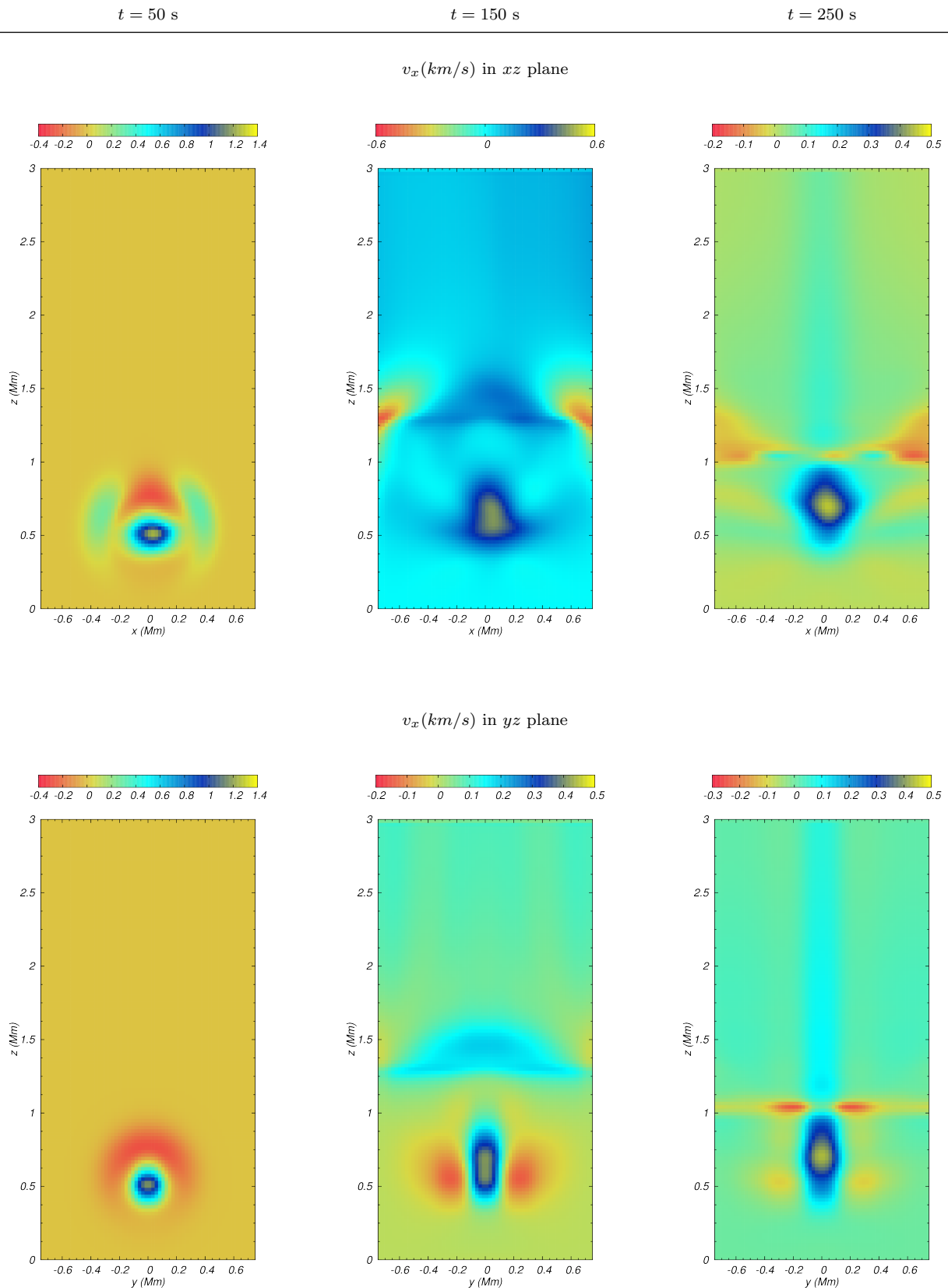


Figure 14. Snapshots of the horizontal component of velocity $v_x(km/s)$ at times $t = 50, 150, 250$ s in the xz and yz planes.

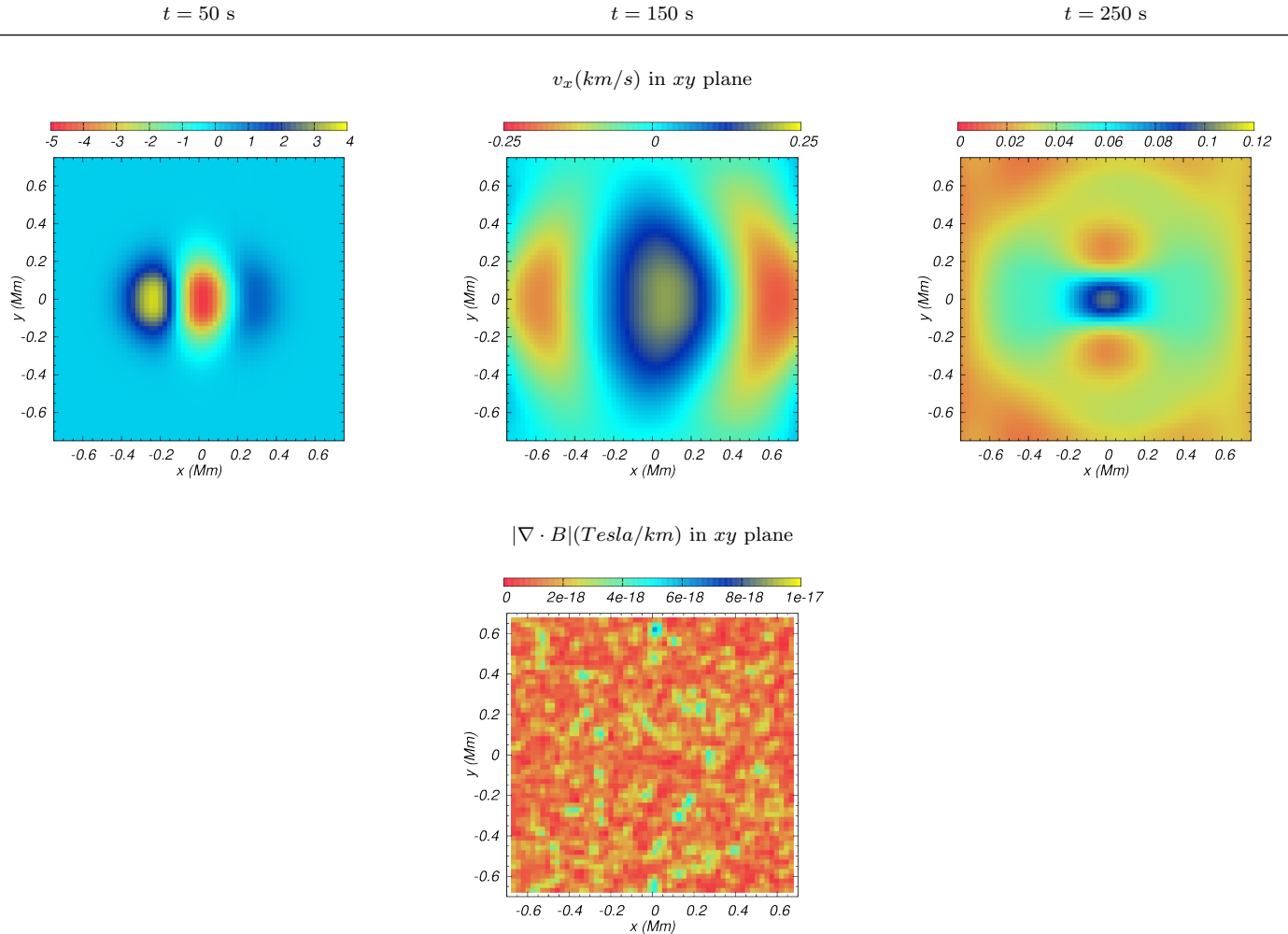


Figure 15. Snapshots of the horizontal component of velocity $v_x (km/s)$ at times $t = 50, 150, 250$ s and $|\nabla \cdot B|$ at $t = 250$ s in the xy plane.

coronal loops in a 2.5D model, in addition we study the propagation of MHD-gravity waves and vortices on a 3D solar atmosphere. These results were compared to previous results in the literature. We have also shown that the constraint has been kept under control.

We have decided to use unigrid mode instead of mesh refinement in order to avoid the use of artificial viscosity at boundaries between refinement levels, which is used to damp out spurious oscillations. We also want to avoid the carbuncle effect at corners of refined grids. In order to carry out production runs with high resolution, we have parallelized our code.

Finally, the code is public and available under request at <http://www.ifm.umich.mx/~cafe>

ACKNOWLEDGMENTS

This research is partly supported by grant CIC-UMSNH-4.9. A. C-O gratefully acknowledges a DGAPA postdoc-

toral grant to Universidad Nacional Autónoma de México (UNAM)

REFERENCES

- Avrett E. H., Loeser R., 2008, ApJS, 175, 229
 Balsara D. S., 2000, Rev. Mex. Astro. Astrof., 9, 72
 Balsara D. S., 2001, ApJS, 132, 83
 Banerjee D., Erdélyi R., Oliver R., O’Shea E., 2007, Sol. Phys., 245
 Brio M., & Wu C. C., 1988, J. Comp. Phys., 75, 400
 Bogdan T. J., et al., 2003, ApJ, 599, 626
 Chmielewski P., Murawski K., Musielak Z.E., Srivastava A.K., 2014, ApJ, 793, 43
 Chmielewski P., Srivastava A.K., Murawski K., Musielak Z.E., 2014, Acta Phys. Pol., 125, 1
 Clarke D. A., 1996, ApJ, 457, 291
 Cruz-Osorio A., Lora-Clavijo F. D., Guzmán F. S., 2012, MNRAS, 426, 732-738
 Cunningham A. J., Frank A., Varniere P., Mitran S., Jones T. W., 2007, astro-ph:0710.0424

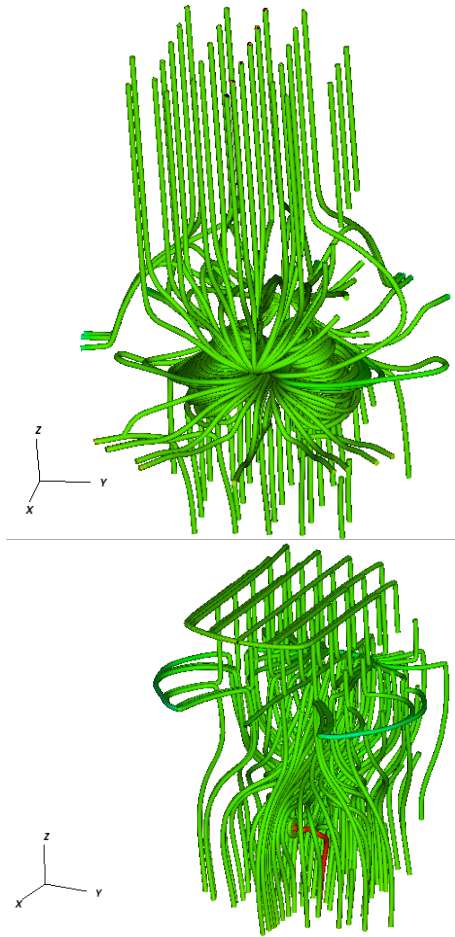


Figure 16. Temporal snapshots of streamlines at $t = 50$ s (top) and $t = 150$ s (bottom) for the case of the horizontal perturbation. Color represents the vorticity magnitude.

- Curdt W., Heinzel P., Schmidt W., Tarbell T., Uexkull V., Wilken V., 1999, ed. A. Wilson (ESA SP-448; Noordwijk: ESA), 177
- Dai W., Woodward P. R., 1998, *ApJ*, 494, 317
- Del Zanna L., Schnaekens E., Velli M., 2005, *A&A*, 431, 1095
- Danilko D., Murawski K., Erdélyi R., 2012, *Acta Phys. Pol.*, 43, 6
- De Pontieu B., McIntosh S. W., Carlsson M., Hansteen V. H., Tarbell T. D., Schrijver C. J., Title A. M., Shine R. A., Tsuneta S., Katsukawa Y., Ichimoto K., Suematsu Y., Shimizu T., Nagata S., 2007, *Sci*, 318, 1574
- DeVore C. R., 1991, *J. Comp. Phys.*, 92, 142
- Einfeldt B., 1988, *SIAM Journal on Numerical Analysis*, 25, 294
- Evans C.R., Hawley J.F., 1988, *ApJ*, 332, 659
- Fedun V., Erdélyi R., Shelyag S., 2009, *Sol. Phys.*, 258, 219
- Frank A., Jones T. W., Ryu D., Gaalaas J., 1996, *ApJ*, 460, 777
- Fromang S., Hennebelle P., Teyssier R., 2006, *A&A*, 457, 371
- Fryxell B., Olson K., Ricker P., Timmes X., Zingale M., Lamb D. Q., Macneice P., Rosner R., Truran J.W., Tufo H., 2000, *ApJS*, 131, 273
- Fuchs F. G., McMurry A. D., Mishra S., Risebro N. H., Waagan K., 2010, *J. Comp. Phys.*, 229, 4033
- Fuchs F. G., McMurry A. D., Mishra S., Waagan K., 2011, *ApJ*, 732
- Gombosi T. I., et al., 2004, *Frontiers Simul.*, 6, 14
- González-Avilés J. J., Guzmán F. S., 2015, *MNRAS*, 451, 4819 arXiv:1505.01401 [astro-ph.SR]
- Harten A., Engquist B., Osher S., & Chakravarthy S. R., 1997, *J. Comp. Phys.*, 131, 3
- Harten P., Lax P. D., Van Leer B., 1983, *SIAM review* 25, 35
- Hawley J. F., Stone J. M., 1995, *Comp. Phys. Comm.*, 89, 127
- Hayes J. C., Norman M. L., Fiedler R. A., Bordner J. O., Li P. S., Clark S. E., ud-Doula A., MacLow M. M., 2006, *ApJS*, 165, 188
- Jain R., Gascoyne A., Hindman B. W., 2011, *MNRAS*, 415, 1276
- Jess D.B., Mathioudakis M., Erdlyi R., Crockett P.J., Keenan F.P., Christian D.J., 2009, *Sci*, 323, 1582
- Konkol P., Murawski K., 2010, *Acta Phys. Pol.*, 41, 6
- Konkol P., Murawski K., Lee D., Weide K., 2010, *A&A*, 521, A34
- Lee D., 2013, *J. Comp. Phys.*, 243, 269
- Lee D., Deane A.E., 2009, *J. Comp. Phys.*, 228, 952
- Londrillo P., Del Zanna L., 2000, *ApJ*, 530, 508
- Lora-Clavijo F. D., Cruz-Osorio A. and Moreno-Mendez, E. 2015, *ApJS* 219, 30 arXiv:1506.08713 [astro-ph.HE]
- Lora-Clavijo F. D., Gracia-Linares M., Guzmán F. S., 2014, *MNRAS*, 3, 443 arXiv:1406.7233 [astro-ph.GA]
- Lora-Clavijo F. D., Guzmán F. S., Cruz-Osorio A., 2013, *JCAP*, 12, 015 arXiv:1312.0989 [astro-ph.CO]
- Lora-Clavijo F. D., Cruz-Perez J. P., Guzmán F. S., Gonzalez J. A., 2013, *Rev. Mex. Fis.*, E 59, 28-50 arXiv:1303.3999 [astro-ph.HE]
- Lora-Clavijo F. D., Guzmán F. S., 2013, *MNRAS*, 429, 3144-3154 arXiv:1212.2139 [astro-ph.HE]
- Lora-Clavijo F. D., Cruz-Osorio A., Guzmán F. S., 2015, *ApJS* 218, 24-58 arXiv:1408.5846 [gr-qc]
- Low B.C., 1985, *ApJ*, 293, 31
- Mignone A., Bodo G., Massaglia S., Matsakos T., Tesileanu O., Zanni C., Ferrari A., 2007, *ApJS*, 170, 228
- Murawski K., Musielak Z. E., 2010, *A&A*, 518, A37
- Murawski K., Srivastava A. K., Zaqarashvili T. V., 2011, *A&A*, 535, A58
- Murawski K., Zaqarashvili T. V., 2010, *A&A*, 519, A8
- Murawski K., Ballai I., Srivastava A. K., Lee D., 2013, *MNRAS*, 436, 1268
- Nool M., Keppens R., 2002, *Comp. Meth. Appl. Math.*, 2, 92
- Nordlund A., Galsgaard K., 1995, *A 3D MHD Code for Parallel Computers* (Tech. Rep. Astron. Obs. Univ. Copenhagen)
- Okamoto T.J., Tsuneta S., Berger T.E., Ichimoto K., Katsukawa Y., Lites B.W., Nagata S., Shibata K., Shimizu T., Shine R.A., Suematsu Y., Shimizu T., Nagata S., 2007, *Sci*, 318, 1574
- Orszag S. A., Tang C. M., 1998, *J. Fluid Mech.*, 90, 129
- Pariat E., Antiochos S. K., DeVore C. R., 2009, *ApJ*, 691, 61
- Pariat E., Antiochos S. K., DeVore C. R., 2010, *ApJ*, 714, 1762
- Pariat E., Dalmasse K., DeVore C. R., Antiochos S. K., Karpen J. T., 2015, *A&A*, 573, A130
- Powell K. G., 1994, *ICASE Report No. 94-24*, Langley, VA
- Powell K. G., Roe P. L., Linde T. J., Gombosi T. I., Zeeuw D. L., 1999, *J. Comp. Phys.*, 153, 284
- Priest E. R., 1982, in *solar Magnetohydrodynamics* (Dordrecht:Reidel)
- Radice D., Rezzolla L., 2012, *A&A*, 547, A26
- Roe P. L., 1986, *Ann. Rev. Fluid Mech.*, 18, 337
- Rosenthal C. S., et al., 2002, *ApJ*, 564, 208
- Ryu D., Jones T. W., 1995, *ApJ*, 228, 258
- Shelyag S., Fedun V., Erdélyi R., 2008, *A&A*, 486, 655
- Shu C. W., Osher S. J., 1989, *J. Comp. Phys.*, 83, 32
- Stone J. M., Norman M. L., 1992, *ApJS*, 80, 753
- Stone J.M., Gardiner T.A., Teuben P., Hawley J.F., Simon J.B., 2008, *ApJS*, 178, 137
- Takahashi K., Yamada S., 2013, *J. of Plasma Phys.*, 335, 356
- Takahashi K., Yamada S., 2014, *J. of Plasma Phys.*, 255, 287
- Titarev V. & Toro E., 2004, *J. Comp. Phys.*, 201, 238
- Tomczyk S., McIntosh S. W., Keil S. L., Judge P. G., Schad T., Seely D. H., Edmondson J., 2007, *Sci*, 317, 1192

Tóth G., 1996, *Astrophys. Lett. & Comm.*, 34, 245
Tóth G., 2000, *J. Comp. Phys.*, 161, 605
Vögler A., Schüssler, 2007, *A&A*, 465, L43
Wolozkiewicz P., Muraswski K., Musielak Z. E., Mignone A.,
2014, *Control and Cybernetics*, 43, 2
Ziegler U., 2005, *A&A*, 435, 385

This paper has been typeset from a \TeX / \LaTeX file prepared
by the author.